# LARGE BINOCULAR TELESCOPE AND *SPITZER* SPECTROSCOPY OF STAR-FORMING GALAXIES AT $1 < z < 3$: EXTINCTION AND STAR FORMATION RATE INDICATORS[*]

W. RUJOPAKARN[1], G. H. RIEKE[1], C. J. PAPOVICH[2], B. J. WEINER[1], J. R. RIGBY[3], M. REX[1], F. BIAN[1],
O. P. KUHN[4], AND D. THOMPSON[4]

[1] Steward Observatory, The University of Arizona, Tucson, AZ 85721, USA; wiphu@as.arizona.edu
[2] George P. and Cynthia Woods Mitchell Institute for Fundamental Physics and Astronomy, Department of Physics and Astronomy,
Texas A&M University, College Station, TX 77843, USA
[3] Observational Cosmology Lab, NASA Goddard Space Flight Center, Greenbelt, MD 20771, USA
[4] Large Binocular Telescope Observatory, The University of Arizona, Tucson, AZ 85721, USA
*Received 2011 October 31; accepted 2012 June 18; published 2012 August 7*

## ABSTRACT

We present spectroscopic observations in the rest-frame optical and near- to mid-infrared wavelengths of four gravitationally lensed infrared (IR) luminous star-forming galaxies at redshift $1 < z < 3$ from the LUCIFER instrument on the Large Binocular Telescope and the Infrared Spectrograph on *Spitzer*. The sample was selected to represent pure, actively star-forming systems, absent of active galactic nuclei. The large lensing magnifications result in high signal-to-noise spectra that can probe faint IR recombination lines, including Paα and Brα at high redshifts. The sample was augmented by three lensed galaxies with similar suites of unpublished data and observations from the literature, resulting in the final sample of seven galaxies. We use the IR recombination lines in conjunction with Hα observations to probe the extinction, $A_v$, of these systems, as well as testing star formation rate (SFR) indicators against the SFR measured by fitting spectral energy distributions to far-IR photometry. Our galaxies occupy a range of $A_v$ from ∼0 to 5.9 mag, larger than previously known for a similar range of IR luminosities at these redshifts. Thus, estimates of SFR even at $z \sim 2$ must take careful count of extinction in the most IR luminous galaxies. We also measure extinction by comparing SFR estimates from optical emission lines with those from far-IR measurements. The comparison of results from these two independent methods indicates a large variety of dust distribution scenarios at $1 < z < 3$. Without correcting for dust extinction, the Hα SFR indicator underestimates the SFR; the size of the necessary correction depends on the IR luminosity and dust distribution scenario. Individual SFR estimates based on the $6.2 \mu m$ polycyclic aromatic hydrocarbon emission line luminosity do not show a systematic discrepancy with extinction, although a considerable, ∼0.2 dex, scatter is observed.

*Key words:* galaxies: evolution – galaxies: high-redshift – galaxies: starburst – infrared: galaxies

*Online-only material:* color figures

## 1. INTRODUCTION

The evolution of the star formation rate (SFR) of galaxies is a central topic to the study of galaxy evolution. It is generally agreed that the SFR density of the universe has declined by an order of magnitude since $z \sim 1$ to the present (e.g., Le Floc'h et al. 2005; Rujopakarn et al. 2010; Magnelli et al. 2011). The exact epoch of the peak of the SFR history is not known precisely, although it appears to be constrained to be within $1 < z < 3$ (e.g., Pérez-González et al. 2005; Reddy et al. 2008; Rodighiero et al. 2010; Magnelli et al. 2011).

At this redshift range, the primary SFR indicators are based on infrared (IR), optical, and extinction-corrected ultraviolet (UV) observations; the resulting SFR estimates commonly disagree with each other by more than a factor of two (e.g., Reddy et al. 2008). The majority of star formation at these redshifts is known to occur in optically extincted star-forming regions in IR luminous galaxies (e.g., Le Floc'h et al. 2005; Dole et al. 2006; Berta et al. 2011), and the uncertainties resulting from the extinction undermine our ability to understand the SFR

history during this era. A better understanding of the SFR history will have important implications on the cosmic stellar mass buildup and metal production. For example, there is a significant discrepancy between the expected metal abundance derived from the SFR history and the observed abundance (Bouché et al. 2007), with some studies indicating the difference to be nearly an order of magnitude, and as a result placing the peak of the SFR history as far back as $z \sim 4$ (Kobayashi et al. 2007).

The situation necessitates more efforts into exploring the nature of optical extinction in high-redshift galaxies using unbiased measures as well as studying the effect of extinction on various SFR indicators.

Extinction measurements based on optical emission lines could be biased in highly obscured environments because the indicator only probes the outer layer of the star-forming regions, where the extinction is relatively low. This effect is observed locally (e.g., Alonso-Herrero et al. 2006), but only because observations are available for longer wavelength IR recombination lines (e.g., Paα and Brα) that are less affected by extinction. In this work, we extend this technique out to $z = 3$ by comparing the strength of the Hα line with those of Paα and Brα. Since the latter are in wavelength regions with 10–20 times less extinction than Hα, they provide a measurement of extinction through the entire star-forming region. With an unbiased estimate of extinction, we can address its effects on SFR indicators in this critical redshift range.

---

In this paper, we study a wide range of star formation diagnostics in seven gravitationally lensed star-forming galaxies at $1 < z < 3$. We observed four of these galaxies spectroscopically with the LUCIFER1 near-IR imaging spectrograph on the Large Binocular Telescope (LBT) to measure the Hα line flux in the near-IR, and with the Infrared Spectrograph (IRS, 5–38 μm) on the *Spitzer Space Telescope* to observe the wavelength regions covering Paα and/or Brα lines as well as aromatic emission lines and emission complexes (commonly attributed to, and hereafter, polycyclic aromatic hydrocarbons or PAHs). The sample comprises A2218b, A2667a, A2218a, and A1835a at redshift 1.03, 1.03, 2.52, and 2.57, respectively (magnification 6×–27×). The IRS observations at longer wavelengths are further used to compare SFR estimates from the 6.2 μm PAH feature. They were carried out under *Spitzer* program ID 82, 30775, and 50586 (PI: G. Rieke); and 40443 and 50372 (PI: C. Papovich). Our sample is augmented by three galaxies with similar suites of observations from unpublished data and the literature: SDSSJ120601+5142 (hereafter the Clone), the Lyman break galaxy LBG MS 1512-cB58 (hereafter cB58), and the 8 O'clock arc, at redshifts 2.00, 2.73, and 2.73, respectively. Our galaxies were also observed with the MIPS instrument (Rieke et al. 2004) on *Spitzer* at 24 and 70 μm by Rigby et al. (2008), allowing us to combine the MIPS data with far-IR photometry from the literature to estimate SFR via $L$(TIR) obtained by fitting the spectral energy distribution (SED) across the peak of the far-IR emission. In addition, we used the 24 μm monochromatic indicator (Rujopakarn et al. 2012) to estimate $L$(TIR).

This paper is organized as follows. We discuss the LBT and *Spitzer* observations and data reduction in Section 2; extinction, metallicity, $L$(TIR), and SFR measurements in Section 3; compare SFR indicators in Section 4; and make concluding remarks in Section 5. We assume a ΛCDM cosmology with $\Omega_m = 0.3$, $\Omega_\Lambda = 0.7$, and $H_0 = 70 \, \text{km s}^{-1} \, \text{Mpc}^{-1}$ throughout this paper.

## 2. OBSERVATIONS AND DATA REDUCTION

Here we describe the selection of our sample (Section 2.1); the spectroscopic observations with LBT/LUCIFER along with the near-IR data reduction (Sections 2.2 and 2.3) and with *Spitzer* (Section 2.4); data compilation from the literature (Section 2.5); and additional photometric observations with *Spitzer* MIPS and the respective data reduction procedure (Section 2.6) that results in the final data set for our sample of galaxies.

### 2.1. Sample Selection

To measure extinction and study its implication on the SFR indicators, we need a sample of star-forming galaxies that we understand very well. Gravitationally lensed galaxies are outstanding candidates because their amplified fluxes and images enable high signal-to-noise (S/N) spectroscopy. The candidates for our new observations were drawn from the pool of objects studied by Rigby et al. (2008). Briefly, the Rigby et al. (2008) selection requires that objects have (1) *Spitzer* MIPS 24 μm flux above 0.4 mJy to be observed efficiently with IRS, (2) morphologies in the optical *Hubble Space Telescope* imaging that exclude members of the lensing cluster, (3) spectroscopic or probable photometric redshift above 1, and (4) lensing magnification above 3×. From the Rigby et al. (2008) sample, we further require that candidates are absent of active galactic nucleus (AGN) activity based on X-ray luminosity below $10^{42} \, \text{erg s}^{-1} \, \text{cm}^{-2}$ and the lack of mid-IR power-law SEDs,

**Table 1**
Sample of High-redshift Strongly Lensed Star-forming Galaxies

| Source | z | R.A. (J2000) | Decl. (J2000) | Lensing Magnification | Reference |
|--------|------|------------|-------------|----------------------|-----------|
| A2218b | 1.034 | 16 35 55.16 | +66 11 50.8 | 6.1 | 1, 2 |
| A2667a | 1.035 | 23 51 40.00 | −26 04 52.0 | 17 | 1, 2 |
| The Clone | 2.003 | 12 06 01.80 | +51 42 30.7 | 27 ± 1 | 3, 5 |
| A2218a | 2.520 | 16 35 54.18 | +66 12 24.8 | 22 ± 2 | 1, 2 |
| A1835a | 2.566 | 14 01 04.96 | +02 52 24.8 | 3.5 ± 0.5 | 1, 2, 6 |
| cB58 | 2.729 | 15 14 22.29 | +36 36 25.7 | ∼30 | 4, 7 |
| 8 O'clock | 2.731 | 00 22 40.97 | +14 31 14.0 | ∼8 | 8, 9 |

**References.** (1) redshifts from our LBT Hα spectroscopy; (2) Rigby et al. 2008; (3) Hainline et al. 2009; (4) Teplitz et al. 2000; (5) Lin et al. 2009; (6) Smail et al. 2005; (7) Seitz et al. 1998; (8) Allam et al. 2007; (9) Finkelstein et al. 2009.

indicating that their 24 μm fluxes are not dominated by AGN emission. Apart from the objects selected from the Rigby et al. (2008) sample, we include three additional objects that match the selection criteria: cB58, the Clone, and the 8 O'clock arc. We will discuss these objects in Section 2.5.

The galaxies in our sample are located behind galaxy clusters that are well modeled for mass distribution. The mass model of the A2218 cluster (Kneib et al. 1996) indicates a magnification value for A2218a of 22 ± 2 (Kneib et al. 2004). For A2218b and A2667a, magnification estimates of 6.1 and 17, respectively, are modeled by Rigby et al. (2008). For A1835a, we adopt the magnification estimate from Smail et al. (2005), 3.5 ± 0.5. The sample is listed in Table 1.

### 2.2. LBT/LUCIFER Near-infrared Spectroscopy

Our near-IR spectroscopy was obtained in three campaigns during 2010 October and 2011 May using the LUCIFER1 instrument on the LBT (Mandel et al. 2007). The common aspects of all these observations are that we use the N1.8 camera with plate scale of 0″.25 pixel$^{-1}$ and with the 210 lines mm$^{-1}$ high-resolution grating, resulting in spectral resolution of 5.0 Å. A-stars were observed for spectrophotometric calibration for each target (details on spectral type below) at similar airmass as the science exposure, either immediately before or after the science exposures. Positions of the LUCIFER slit for each of our observations are shown in Figure 1.

A2667a was observed on 2010 November 3 in the long-slit spectroscopy mode using a slit of 1″.5 by 3.9 arcmin under variable seeing of 1″.2–2″.5. The slit was rotated to P.A. = 320° to place it along the length of the lensed arc. The total integration time was 12 × 300 s with the telescope nodded 50″ along the slit. The unusually long nodding was required by the ∼25″ length of the arc. For calibration, we observed HD 223466, an A3V calibration star with V = 6.42 mag, through the same setup using a total integration time of 2 × 20 s in two nodding positions.

A2218b was observed on 2011 March 10 in the long-slit spectroscopy mode using a slit of 1″.0 by 3.9 arcmin under 0″.4–0″.5 seeing. The slit was rotated to P.A. = 42°.5 to place it along the lensed arc, which is ∼20″ long. The arc is 1″.9 wide in the widest region; thus, we took the spectra at the central position and another position shifted by 0″.9, with the 0″.1 overlapping allowing for possible pointing errors to prevent a gap in the slit mapping. We will refer to these positions as the "Central" and the "Central + 0″.9" positions, respectively. The total integration time was 6 × 300 s at the Central position and 5 × 300 s at the Central + 0″.9 position, totalling 55 minutes, with the telescope
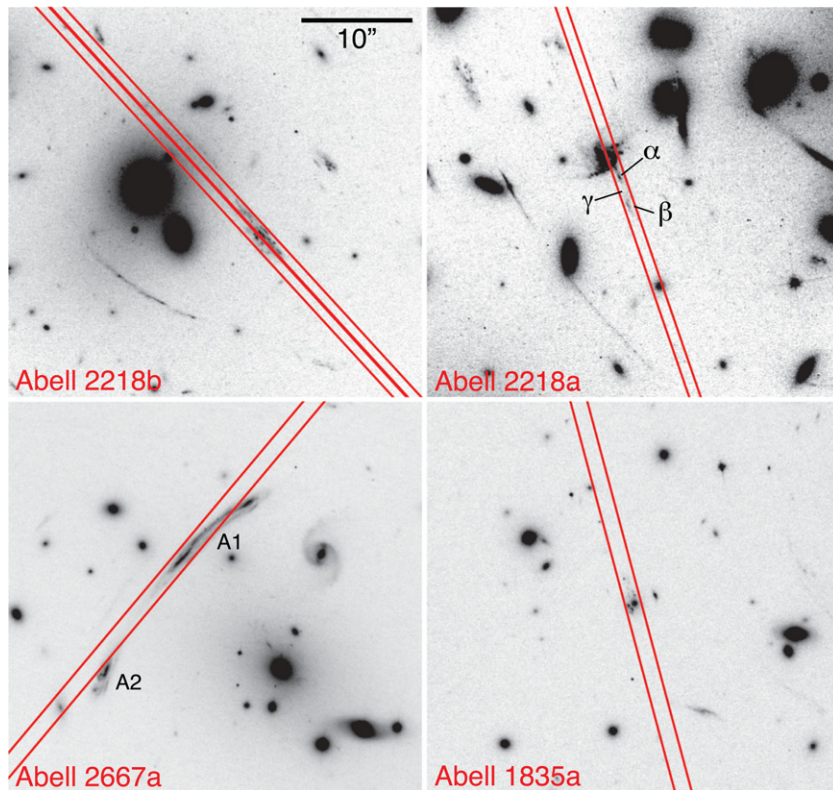
**Figure 1.** Images of the lensed galaxies in our sample from the *Hubble Space Telescope* Advanced Camera for Survey (ACS) with the positions of our LBT/LUCIFER slit for NIR spectroscopy shown in red. Clockwise from top left are A2218b, A2218a, A1835a, and A2667a. The ACS filter for A2218a and A2218b is F625W; A1835 and A2667 images were taken in F850LP. Each image is 37″ wide (identical scale in all four panels), north is up, east is left. For A2218a and A2667a, each lensed component is labeled following Kneib et al. (2004) and Sand et al. (2005), respectively.

(A color version of this figure is available in the online journal.)

nodded $40''$ along the slit for both. An A0V calibration star, HD 145454, with $V = 5.43$ mag was observed using a total integration time of $2 \times 20$ s in two nodding positions.

A2218a was observed on 2011 March 11 in the long-slit spectroscopy mode using a slit of $1''0$ by 3.9 arcmin under $0''9$–$1''1$ seeing. The slit was rotated to P.A. = $18°9$ to place it along the lensed arc. The total integration time was $10 \times 300$ s with the telescope nodded $20''$ along the slit. We observed the same calibration star as for A2218b.

A1835a was observed on 2011 May 7 in the long-slit spectroscopy mode using a slit of $1''5$ by 3.9 arcmin under $1''0$–$1''1$ seeing. The slit was rotated to P.A. = $15°0$ to place it along the length of A1835a. The total integration time was $12 \times 300$ s with the telescope nodded $20''$ along the slit. An A2V calibration star, HD 122365, with $V = 5.98$ mag was observed using a total integration time of $2 \times 20$ s in two nodding positions.

We took Ar lamp exposures for wavelength calibration along with dark and flat exposures during daytime.

### 2.3. LBT/LUCIFER Data Reduction

Our near-IR spectral reduction has four steps: sky subtraction, spectral extraction, flux calibration, and line flux measurements. We first use a modified version of an IDL long-slit reduction package written by G. D. Becker for NIRSPEC (Becker et al. 2009) to perform sky subtraction following the prescription of Bian et al. (2010). The sky-subtracted two-dimensional spectra are corrected for the two-dimensional dispersion distortions, wavelength calibrated, and extracted using IRAF. We note that the flexure compensation mechanism of LUCIFER1 was not

available during our campaigns, but clean sky subtraction was achieved with the reduction procedure. We combine spectra for each object by averaging values within each wavelength element with sigma clipping at $2.5\sigma$ and then flux calibrate using the `xtellcor_general` tool (Vacca et al. 2003) and the A-star calibrators described in the previous section. Line fluxes for our objects are measured by integrating the line and subtracting the background estimated from the mean continuum in the spectral range. We estimate the line flux uncertainties by a Monte Carlo simulation done by repeatedly ($n = 10^4$) simulating the object's spectrum using random values drawn from the Gaussian distribution centered at the observed flux and $\sigma$ equal to the observed uncertainties and repeat the line measurement. We take the resulting $1\sigma$ distribution of the simulated line flux values to be the uncertainties for the line flux.

### 2.4. Spitzer IRS Mid-infrared Spectroscopy and Data Reduction

Unpublished *Spitzer* IRS spectroscopy in this work is from (1) *Spitzer* program 50586 (PI: G. Rieke) to take deep (integration times ∼15 ks) first-order short–low spectra (SL1; 7.4–14.5 $\mu$m) in the Br$\alpha$ wavelength regions of A2667a and A2218b; and (2) *Spitzer* program 40443 (PI: C. Papovich) to take deep (integration time 7–14 ks) second-order short–low spectra (SL2; 5.2–7.7 $\mu$m) in the Pa$\alpha$ wavelength regions of A2218a and A1835a. For each of the four objects, the IRS first-order long–low spectra (LL1; 19.5–38.0 $\mu$m) were from GTO programs 82 (A2218a and A1835a) and 30775 (A2218b and A2667a), PI: G. Rieke. The IRS second-order long–low spectra (LL2; 14.0–21.3 $\mu$m) are available for A2218b and
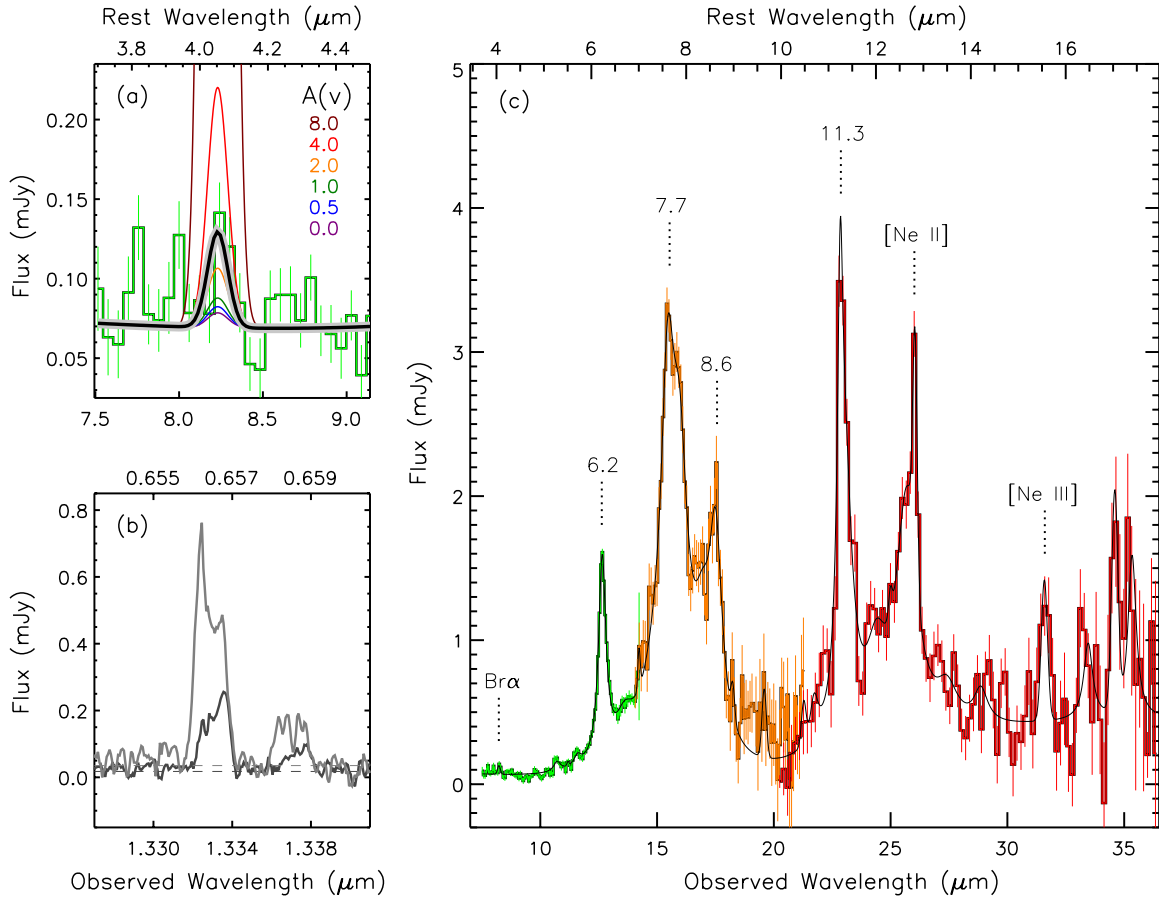
**Figure 2.** *Spitzer*/IRS mid-IR and LBT/LUCIFER near-IR spectra of A2218b. Panel (a) is the magnified region of IRS SL1 spectrum at the Brα wavelength. The best Gaussian fit to the Brα emission line is the thick black line. The color-coded Gaussians at the Brα line wavelength illustrate the expected Brα line flux for each extinction scenario from $A_v$ of 0 to 8.0 mag given the observed Hα flux. Panel (b) shows the Hα emission line from LBT/LUCIFER. The light and dark gray spectra are extracted from the two parallel slit positions shown in Figure 1. A double-peak line profile is clearly visible. The continuum level for each aperture is shown as dashed lines. Panel (c) presents the overall IRS spectra with the green, orange, and red lines representing spectrum from the IRS SL1, LL2, and LL1 modules, respectively.

(A color version of this figure is available in the online journal.)

**Table 2**
Near- and Mid-infrared Spectroscopic Observations

| Source | IRS Exposure Time (ks) | | | | IRS Program ID | Near-IR Spectroscopy |
|---|---|---|---|---|---|---|
| | SL2 | SL1 | LL2 | LL1 | | |
| A2218b | . . . | 15.1 | 3.6[a] | 3.6[a] | 30775, 50586 | This work |
| A2667a | . . . | 16.1 | 1.9[a] | 1.9[a] | 30775, 50586 | This work |
| The Clone | 8.6 | . . . | 21.6[b] | 20.9[b] | 40430, 50372 | Hainline et al. (2009) |
| A2218a | 14.4[c] | . . . | . . . | 3.6[a] | 82, 40443 | This work |
| A1835a | 7.7 | . . . | . . . | 3.6[a] | 82, 40443 | This work |
| cB58 | 6.8[d] | 6.8[d] | 14.6[c] | 34.1[c] | 30832 | Teplitz et al. (2000) |
| 8 O'clock | 14.4 | . . . | . . . | 22.1 | 40443 | Finkelstein et al. (2009) |

**Note.** *Spitzer* IRS spectra previously published in (a) Rigby et al. (2008), (b) Fadely et al. (2010), (c) Papovich et al. (2009), and (d) Siana et al. (2008).

A2667a from program 30775, and A1835a from program 82. These data are published in Rigby et al. (2008). The details of IRS observations for our sample are summarized in Table 2.

We have reduced all archival spectroscopic data for objects in our sample using the most updated version of the processing software from Level-1 data (BCD) for IRS by following the prescription of Teplitz et al. (2007). Briefly, first we use IRAF to fit the background slope with time for each row and subtract that fitted value row by row to remove latent charge. Second, we interpolate over bad and/or hot ("rogue") pixels using the IDL routine IRSCLEAN (version 2.1) provided by the SSC based on

the known hot pixel mask for the corresponding campaign, plus manual identification. Third, we subtract sky using a sky image constructed from a median of other map positions. Then we co-add each map position into a two-dimensional (2D) spectrum and use the SPICE software (version 2.4) provided by the SSC to extract a one-dimensional (1D) spectrum using the optimal extraction template for point sources for each map position. The 1D spectra are combined with sigma clipping at $2.5\sigma$ into the final 1D spectra shown in Figures 2 and 3.

We use the PAHFIT package (Smith et al. 2007) to measure PAH feature fluxes. PAHFIT uses $\chi^2$ minimization to simulta-
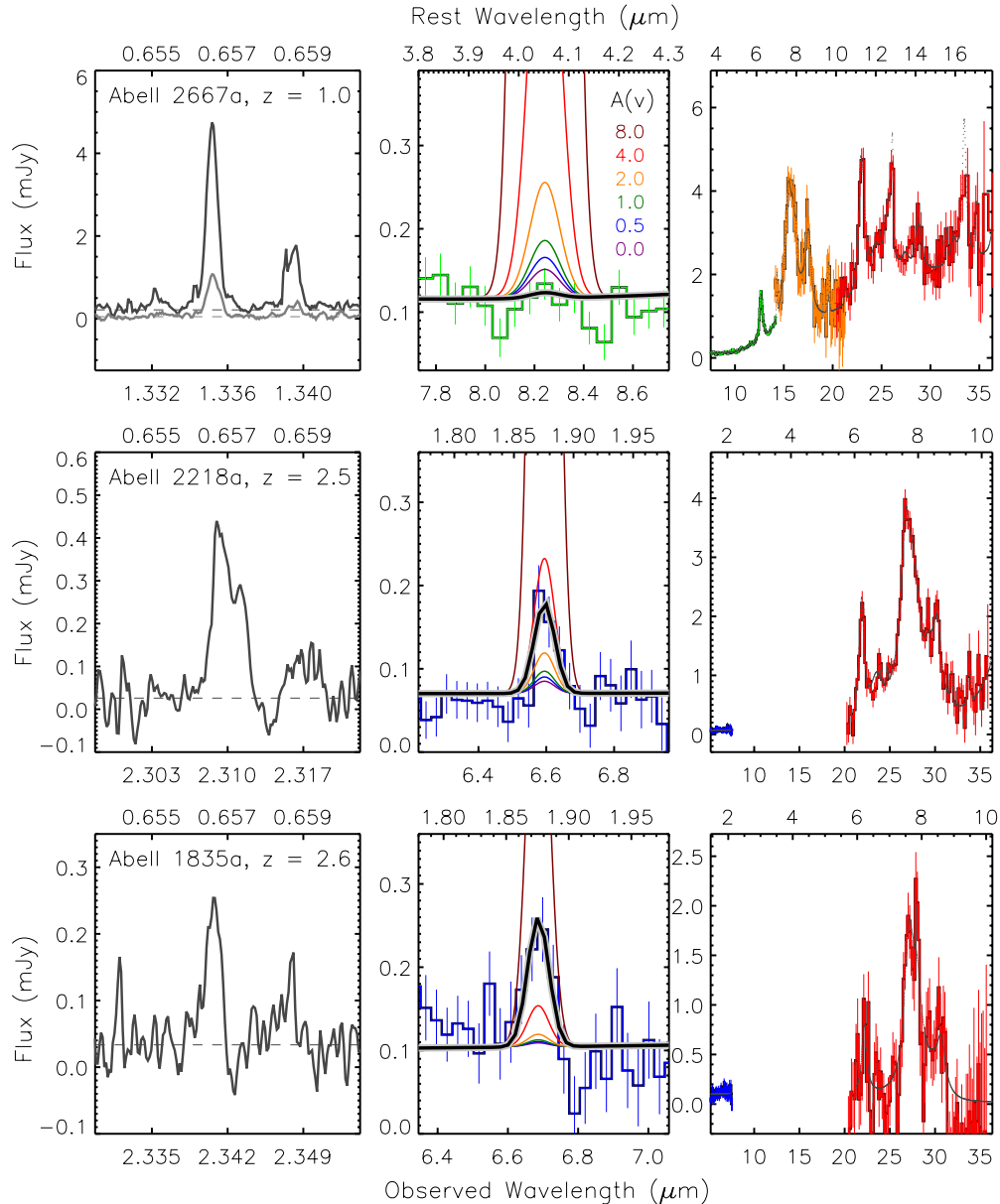
**Figure 3.** Same as Figure 2 but for A2667a, A2218a, and A1835a, from top to bottom, respectively. The IRS SL2 module spectra (not available for A2218b in the previous figure), which cover Paα lines for A2218a and A1835a, are shown in blue. There is no SL1 and LL2 coverage for A2218a and A1835a.

(A color version of this figure is available in the online journal.)

neously fit the PAH and nebular emission lines, stellar and dust continua, as well as the silicate absorption feature. We report the PAH flux measurements in Table 3. To define the dust and stellar continuum for the measurement of Paα and/or Brα line fluxes, we iteratively fit the IRS spectra with PAHFIT and interpolate over points with fit residuals greater than $3\sigma$. This process is repeated until there are no remaining outliers (usually within the third iteration) and the final fit, which is effectively a noise-free template representing the object's spectrum, is adopted as a continuum estimate. The actual line flux measurements for both the PAH emissions and recombination lines are done on the original spectra, i.e., only the continua for IR recombination line measurements are determined with this iterative fitting procedure. This method of continuum estimation allows construction of a mid-IR spectral template that best matches each galaxy in a non-parametric manner. In other words, it provides continuum estimates in the Paα and Brα wavelength regions that

are not only constrained by photometric observations (e.g., from *Spitzer*/IRAC), but also by PAH-region information. These continuum estimates are shown for each object in Figures 2–4.

Brα and Paα lines are measured by fitting Gaussian profiles with widths fixed at the resolution of the IRS module covering the line, the central wavelengths fixed at the expected line wavelengths based on the optical spectroscopic redshift, and the Gaussian base given by the continuum under the expected wavelength range of the line; the line peak is the only free parameter to fit. The line flux uncertainties are estimated by a procedure similar to that of the Hα line flux uncertainties: (1) a series of spectra ($n = 10^4$) were generated randomly based on the actual spectra and the $\sigma$ uncertainties, (2) line flux measurements are carried out on them, and (3) we take the $1\sigma$ value of the simulated flux distribution to be the uncertainties for the line flux. If the formal fit to the line yields negative line flux due to non-detection (occurring in two cases, cB58 and the
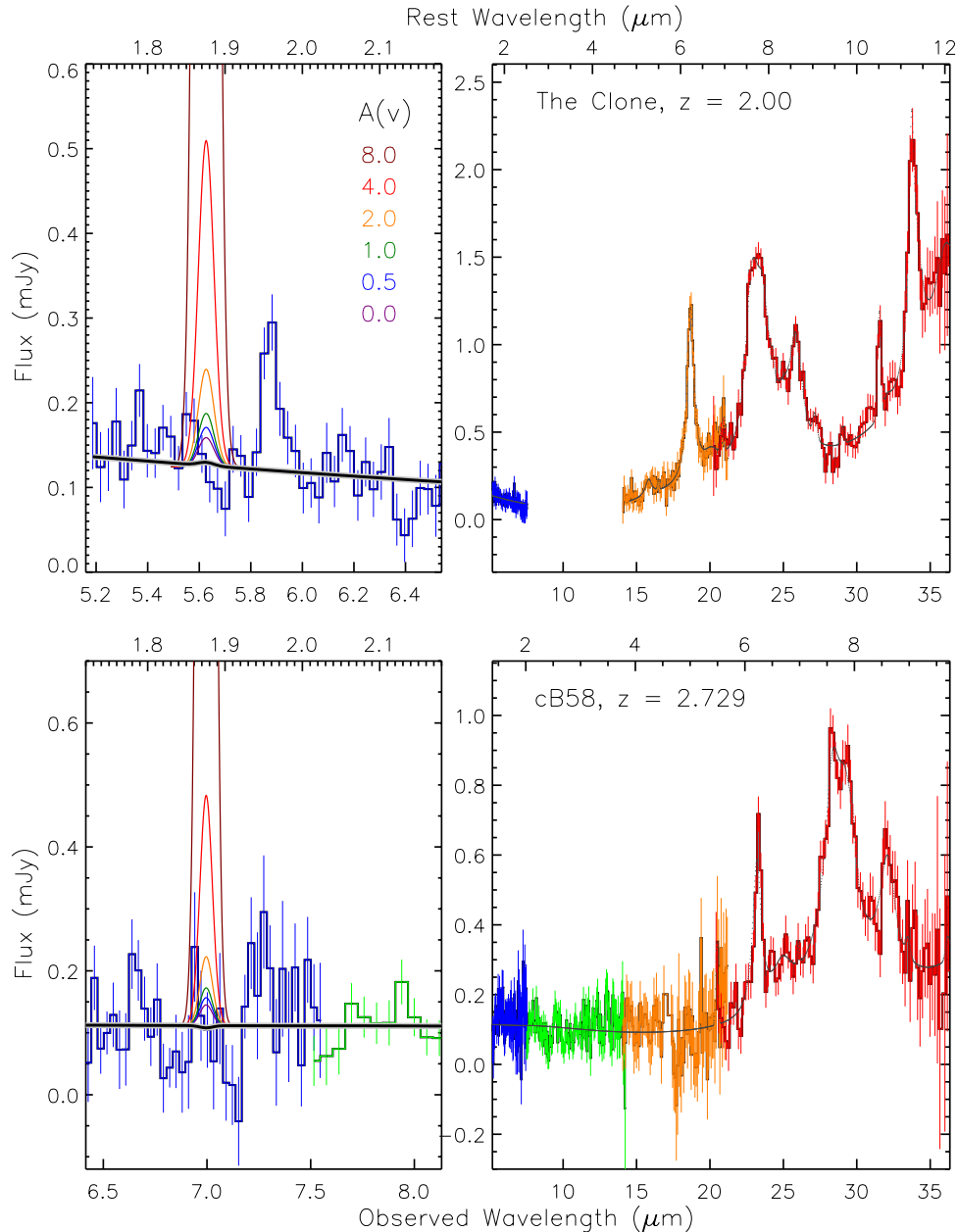
**Figure 4.** Our reduction of the *Spitzer* IRS spectra for the Clone (SDSSJ1206+5142) and cB58 (cf. Fadely et al. 2010 and Siana et al. 2008, respectively). The color coding for IRS modules the line fluxes for each $A_v$ scenario is the same as Figures 2 and 3. We note that the apparent spectral feature at ~5.9 μm (observed frame) in the SL2 spectrum of the Clone cannot be interpreted as a Paα line at the redshift $z = 2.00$, which has been measured from multiple optical lines (see discussion in Section 3.1).

(A color version of this figure is available in the online journal.)

Clone), we adopt the $1\sigma$ value as an upper limit to the line flux. The measurements are reported in Table 4.

### 2.5. Archival and Literature Data

We augmented our sample with three additional objects: the Clone, cB58, and the 8 O'clock arc. These objects have suites of data similar to our sample: rest-frame optical spectroscopy covering Hα and deep IRS spectroscopy covering Paα (Table 1).

cB58 (Yee et al. 1996), at redshift $z = 2.729$, is the first lensed LBG known with high magnification (~30×); it has been studied extensively from UV to millimeter wavelengths (Siana et al. 2008, and references therein). Rest-frame optical spectroscopy was obtained by Teplitz et al. (2000). Siana et al.

(2008) present a full suite of IRS observation (SL2, SL1, LL2, and LL1) for the galaxy. We re-reduced these IRS data using our procedure above and found the result to be consistent with the original reduction published in Siana et al. (2008); details are given in Section 3.1. The lensing magnification of cB58, ~30×, was from Seitz et al. (1998).

The Clone, at redshift $z = 2.0026$, was discovered from SDSS imaging (Lin et al. 2009). Its rest-frame optical spectroscopy was obtained by Hainline et al. (2009). IRS observations in the LL2 and LL1 bands were obtained by Fadely et al. (2010), who concluded that the Clone's IR emission is dominated by a starburst based on the strength of the 6.2 μm PAH feature, despite the object showing a very strong [S IV] emission line. The Clone's deep IRS SL2 observation is a part

**Table 3**
Measured PAH Fluxes

| Source | $f(\mathrm{PAH}_{6.2})$ | $f(\mathrm{PAH}_{7.7\ \mathrm{Complex}})$ | $f(\mathrm{PAH}_{8.6})$ | $f(\mathrm{PAH}_{11.3\ \mathrm{Complex}})$ | $f(\mathrm{PAH}_{12.6})$ |
|---|---|---|---|---|---|
| A2218b | $15.9 \pm 0.2$ | $72.2 \pm 1.8$ | $13.2 \pm 1.0$ | $17.3 \pm 0.7$ | $12.7 \pm 0.9$ |
| A2667a | $13.0 \pm 0.2$ | $82.1 \pm 3.0$ | $19.9 \pm 2.2$ | $21.6 \pm 1.3$ | $11.7 \pm 1.6$ |
| The Clone | $7.5 \pm 0.3$ | $15.9 \pm 0.4$ | $4.2 \pm 0.3$ | $4.5 \pm 0.7$ | . . . |
| A2218a | $16.0 \pm 0.8$ | $54.4 \pm 1.3$ | $10.3 \pm 0.8$ | . . . | . . . |
| A1835a | $7.5 \pm 1.4$ | $26.1 \pm 1.6$ | $7.5 \pm 1.9$ | . . . | . . . |
| cB58 | $2.9 \pm 0.2$ | $9.7 \pm 0.5$ | $2.5 \pm 0.4$ | . . . | . . . |

**Notes.** PAH emission lines and emission complex fluxes measured by PAHFIT in $10^{-15}\ \mathrm{erg\ s^{-1}\ cm^{-2}}$. These values are not corrected for lensing magnification. Dots indicate that the feature is outside spectral coverage. The 7.7 $\mu$m and 11.3 $\mu$m complexes are the sum of fluxes at wavelength 7.3–7.9 $\mu$m and 11.2–11.4 $\mu$m, respectively. The LL2 spectrum of the 8 O'clock arc does not have sufficient S/N to measure PAH line fluxes consistently.

**Table 4**
Measured Fluxes

| Source | $f(24\ \mu\mathrm{m})$ (1) | $f(70\ \mu\mathrm{m})$ (2) | $f(\mathrm{H}\alpha)$ (3) | $f([\mathrm{N\ II}]\ 6583)$ (4) | $f(\mathrm{Pa}\alpha)$ (5) | $f(\mathrm{Br}\alpha)$ (6) | $f[\mathrm{Ne\ II}\ 12.8]$ (7) | $f[\mathrm{Ne\ III}\ 15.5]$ (8) |
|---|---|---|---|---|---|---|---|---|
| A2218b | 1.67 | $7.4 \pm 1.5$ | $21.2 \pm 0.6$ | $5.2 \pm 0.5$ | . . . | $4.3 \pm 0.9$ | $1.8 \pm 0.2$ | $0.9 \pm 0.2$ |
| A2667a | 4.52 | $19.4 \pm 3.9$ | $78.7 \pm 1.5$ | $31.1 \pm 3.2$ | . . . | $0.4 \pm 1.0$ | $2.8 \pm 0.4$ | $0.9 \pm 0.3$ |
| The Clone | 0.88 | $8.8 \pm 1.8$ | $20.2 \pm 0.5^{\mathrm{a}}$ | $3.9 \pm 0.2^{\mathrm{a}}$ | $<1.3$ | . . . | . . . | . . . |
| A2218a | 1.16 | $<7$ | $6.2 \pm 0.3$ | $1.5 \pm 0.3$ | $5.7 \pm 1.2$ | . . . | . . . | . . . |
| A1835a | 0.99 | $<13$ | $1.8 \pm 0.3$ | $1.0 \pm 0.3$ | $7.9 \pm 1.5$ | . . . | . . . | . . . |
| cB58 | $0.24^{\mathrm{b}}$ | $1.7 \pm 1.0^{\mathrm{b}}$ | $12.6 \pm 0.4^{\mathrm{c}}$ | $1.1 \pm 0.3^{\mathrm{c}}$ | $<2.3$ | $<1.3$ | . . . | . . . |
| 8 O'clock | 0.57 | . . . | $17.6 \pm 0.5^{\mathrm{d}}$ | $4.8 \pm 0.4^{\mathrm{d}}$ | $11.5 \pm 2.2$ | . . . | . . . | . . . |

**Notes.** Column 1: 24 $\mu$m flux in mJy. $f(24\ \mu\mathrm{m})$ of Abell galaxies except A2667a are from Rigby et al. (2008), who noted that DAOPHOT errors of the flux are overly optimistic and thus not reported. A nominal uncertainty of 0.1 mJy is adopted for SED fitting for $L(\mathrm{TIR})$. Rigby et al. (2008) mistakenly reported an $f(24\ \mu\mathrm{m})$ for only one component of the A2667 arc. A correct value is reported here. Column 2: 70 $\mu$m flux in mJy. Columns 3 and 4: optical line fluxes in $10^{-16}\ \mathrm{erg\ s^{-1}\ cm^{-2}}$. Columns 5 and 6: IR recombination lines fluxes in $10^{-16}\ \mathrm{erg\ s^{-1}\ cm^{-2}}$. The formal fit to the Br$\alpha$ line of cB58 yields a flux value of $(-0.4 \pm 1.3) \times 10^{-16}\ \mathrm{erg\ s^{-1}\ cm^{-2}}$ and hence a 1$\sigma$ limit is reported in the table. Also for the Pa$\alpha$ line, the formal fit yields $(-0.2 \pm 2.3) \times 10^{-16}\ \mathrm{erg\ s^{-1}\ cm^{-2}}$ and hence the 1$\sigma$ limit is reported. Likewise, a 1$\sigma$ limit is reported for the Pa$\alpha$ line flux of the Clone, where a formal fit yields $(0.3 \pm 1.3) \times 10^{-16}$. Columns 7 and 8: line fluxes of [Ne II] 12.8 $\mu$m and [Ne III] 15.5 $\mu$m in $10^{-15}\ \mathrm{erg\ s^{-1}\ cm^{-2}}$ measured by PAHFIT. Dots indicate no spectral coverage. These values are not corrected for lensing magnification. Flux references: (a) Hainline et al. (2009); (b) Siana et al. (2008); (c) Teplitz et al. (2000); (d) Finkelstein et al. (2009).

of *Spitzer* program 50372 (PI: C. Papovich) with an integration time of 8.6 ks. As with cB58, we re-reduced all IRS data using our procedure and software to ensure consistency. We present our reduction of these archival data in Figure 4. The lensing magnification for the Clone, $27 \pm 1\times$, was reported by Lin et al. (2009).

The 8 O'clock arc at redshift $z = 2.7308$ was discovered serendipitously from SDSS imaging by Allam et al. (2007). Finkelstein et al. (2009) obtained the rest-frame spectroscopy of components "A2" and "A3" in the nomenclature of Allam et al. (2007). The arc was observed as a part of *Spitzer* program 40443 (PI: C. Papovich) with an SL2 integration time of 14.4 ks. The slit for the SL2 observation is centered on the "A2" component and covered significant parts of both the "A1" and "A3" components such that any bias due to spatial variation of recombination lines along the lensed arc will be negligible. The PAH spectrum of the 8 O'clock arc shows 6.2 $\mu$m and 7.7 $\mu$m emission features, yet at low S/N due to contamination in the IRS slit from a nearby IR-bright dust-obscured galaxy, which we will discuss in the next section. We adopt the magnification estimate of 8× for the arc (Finkelstein et al. 2009).

### 2.6. Additional Spitzer MIPS Photometry and Data Reduction

The *Spitzer* MIPS 24 and 70 $\mu$m photometry for objects behind the Abell clusters are taken from Rigby et al. (2008) with exception of A2667a, whose 70 $\mu$m photometry is reported as an upper limit in Rigby et al. (2008) but which was re-observed with longer integration time in *Spitzer* program ID 50586 (PI:

G. Rieke). For the Clone, we downloaded the 24 and 70 $\mu$m data observed as part of programs 40430 (PI: S. Allam) and 50372 (PI: C. Papovich). The *Spitzer* MIPS observations for the 8 O'clock arc were obtained under program 40443 (PI: C. Papovich).

We measured the 24 and 70 $\mu$m fluxes from the Level-2 (PBCD) data using the `Starfinder` IDL routine (Diolaiti et al. 2000) to perform PSF photometry. The PSF model was generated using the `STinyTim` routine provided by the SSC and smoothed according to a prescription given by Engelbracht et al. (2007) to better match the observed PSF. We require $\sigma = 3$ and the PSF correlation value of 0.75 for our 24 and 70 $\mu$m flux measurements. The 8 O'clock arc has a 24 $\mu$m bright dust-obscured galaxy $\sim6\farcs5$ away that partially blends with the arc, but we were able to deblend the flux by performing PSF photometry to subtract the intervening source first and repeat the photometry to measure the flux of the arc. This contaminating galaxy is highly extincted, such that it is undetected in the SDSS imaging and was discovered only in the 24 $\mu$m observation. Our flux measurements along with fluxes from the literature are reported in Table 4.

### 2.7. Augmented Sample Summary

Our augmented sample consists of the four galaxies we observed plus the three from the literature. In addition to the measurements of H$\alpha$ and of at least one of the IR recombination lines (Pa$\alpha$ and/or Br$\alpha$), all of them have good 24 $\mu$m photometry, far-IR and sub-millimeter photometry as well as

IRS spectroscopy covering, at least, the 6–8 $\mu$m wavelength region. The IRS coverage goes out to nearly 17 $\mu$m (rest frame) in the two lowest redshift objects (A2667a and A2218b, $z \sim 1.0$).

## 3. RESULTS

In this section, we describe the near- and mid-IR spectra and the derived physical quantities, including metallicity, $L$(TIR), and SFR from optical and IR tracers, and extinction measurements.

### 3.1. Near- and Mid-IR Spectroscopy

The final 1D H$\alpha$ spectra from our LBT/LUCIFER1 observations are shown in Figures 2 and 3 along with the IRS spectra. The 6.2 $\mu$m PAH emission line, 7.7 $\mu$m complex, and 8.6 $\mu$m complex are clearly detected in all galaxies.

The spectra from both slit positions (Section 2.2) of A2218b show highly asymmetric line profiles. The profile at the central position is double-peaked in both H$\alpha$ and [N II] while the Central + 0″9 spectrum shows a single-sided profile with stronger emission at the red side of the line. The combined line profile from both slit positions is well fitted with a double Gaussian, whose deconvolved spectral width (corrected for instrumental resolution) indicates a velocity dispersion of $163 \pm 3$ km s$^{-1}$. Traces of the arc northeast of the main component hinted in the ACS image are not detected at H$\alpha$. The IRS spectrum for A2218b shows a strong [Ne III] 15.56 $\mu$m line as well as the [Ne II] line at 12.81 $\mu$m, apart from other PAH features. The Br$\alpha$ line is detected at 4.8$\sigma$ with line flux of $(4.3 \pm 0.9) \times 10^{-16}$ erg s$^{-1}$ cm$^{-2}$.

The spectra of A2667a were extracted from two apertures in the slit. Both of these positions are very bright in H$\alpha$. Referring to Figure 1, these apertures are at (1) the main arc north–northeastern of the brightest cluster galaxy (BCG, identified as "A1" by Sand et al. 2005, and in Figure 1); and (2) the smaller arc east of the BCG (the "A2" arc in the Sand et al. study). Although it appears that a part of the smaller arc is outside the slit in the optical image, the H$\alpha$ line is clearly detected (the light gray spectrum in Figure 3, top row, left column). Both apertures show the same profile for both H$\alpha$ and [N II] lines. No velocity shift between the two components is observed. The formal fit to the Br$\alpha$ line yields a flux of $(0.4 \pm 1.0) \times 10^{-16}$, a non-detection. The galaxy has the warmest dust continuum among our samples, as seen in the rising SED toward the red end of the IRS spectrum in Figure 3 (cf. A2218b's continuum in Figure 2). However, the strong PAH emission is inconsistent with the system's emission being dominated by an AGN in the mid-IR. Its log([N II]/H$\alpha$) line ratio of $-0.40$ alone (i.e., without the [O III] and H$\beta$) does not unambiguously support or rule out the presence of a weak narrow-line AGN. But even with the presence of a weak, optically selected AGN, the EW of the 6.2 $\mu$m PAH emission could still serve as a good tracer of SFR because the suppression of PAH emission due to AGN is found to be limited to the nuclear region (Diamond-Stanic & Rieke 2010).

The H$\alpha$ line of A2218a also shows a double-peaked profile indicating a velocity dispersion of $188 \pm 5$ km s$^{-1}$. The galaxy has been a subject of a previous near-IR spectroscopic study by Richard et al. (2011). Our slit orientation, however, is different (see their Figure 1); they excluded the $\beta$ and $\gamma$ components (the former being a major component) in the nomenclature of Kneib et al. (2004), as shown in Figure 1, while our slit orientation covers all the main components ($\alpha$, $\beta$, and $\gamma$). The



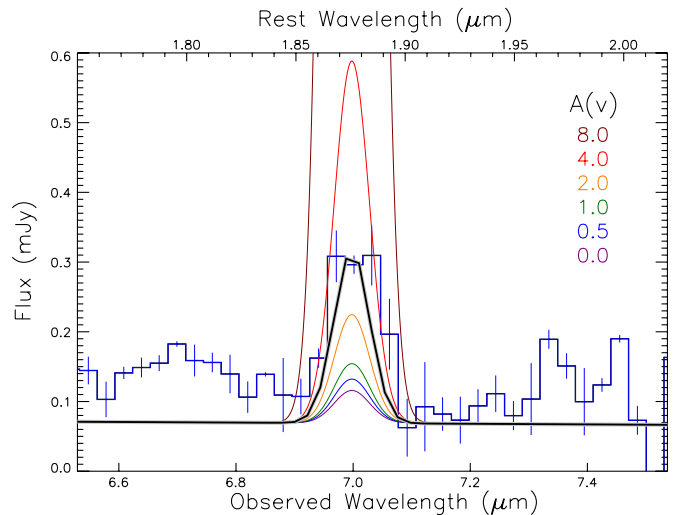**Figure 5.** *Spitzer* IRS SL2 spectrum for the 8 O'clock arc, showing the Pa$\alpha$ line. The color coding for IRS module and the line fluxes for each extinction scenario are the same as Figures 2–4.
(A color version of this figure is available in the online journal.)

Pa$\alpha$ observation, which targets the $\beta$ component, detected Pa$\alpha$ line at 4.8$\sigma$ with line flux of $(5.7 \pm 1.2) \times 10^{-16}$ erg s$^{-1}$ cm$^{-2}$. This measurement is consistent with the previously published reduction of the same data by Papovich et al. (2009), who measured the line flux to be $(8.5 \pm 1.4) \times 10^{-16}$ erg s$^{-1}$ cm$^{-2}$. We attribute the small difference in the two measurements to the different definition of the continuum: Papovich et al. (2009) defined their continuum with IRAC photometry whereas our reduction adopted the simultaneous multi-component fit of spectral features described in Section 2.4.

A1835a shows a faint H$\alpha$ line, too faint to measure asymmetry in the line profile, but a bright Pa$\alpha$ line with a flux of $(7.9 \pm 1.5) \times 10^{-16}$ erg s$^{-1}$ cm$^{-2}$. This is the second brightest Pa$\alpha$ detection in our sample, after the 8 O'clock arc, whose Pa$\alpha$ flux is $(11.5 \pm 2.2) \times 10^{-16}$ erg s$^{-1}$ cm$^{-2}$. The LL1 PAH spectrum of the 8 O'clock arc does not have sufficient S/N to use PAHFIT to construct a noise-free spectrum as a template for the Pa$\alpha$ line flux measurement (Section 2.4) due to the contamination from the nearby IR-bright dust-obscured galaxy, thus instead the continuum of the arc for the measurement is defined by interpolating between the IRAC 5.0 and 8.0 $\mu$m photometric points. These IRAC observations yield fluxes of $74 \pm 3$ and $64 \pm 4$ $\mu$Jy for the 5.8 and 8.0 $\mu$m bands, respectively. We present the Pa$\alpha$ spectrum of the 8 O'clock arc in Figure 5.

For the two IRS spectra from the literature, the Clone and cB58, our reduction generally agrees with those published previously by Fadely et al. (2010) and Siana et al. (2008), respectively. Small differences are noted in the PAH line fluxes due to the way that the continuum for the fit is defined. PAHFIT uses multi-component dust features to represent the continuum, while a single-component power law is used by Fadely et al. and Siana et al. Their approach resulted in a similarly good fit to the data compared to ours, although the measured PAH flux could differ, as observed in the Clone's PAH fluxes from the 6.2–11.3 $\mu$m features where the Fadely et al. (2010) values are a factor of 2.6–3.7 larger than ours. Fadely et al. reported that their results are a factor of 1–8 higher than those of Brandl et al. (2006) in their re-reduction of the same data set. Brandl et al. use a continuum level defined on either side of the emission features and thus their PAH fluxes will be systematically smaller than

with either our PAHFIT measurement or the single-component continuum method. That is, we expect the measurements of the PAH line flux from the same data to yield flux values in the following increasing order: Brandl et al., PAHFIT, and Fadely et al./Siana et al., which is consistent with the differences we find. The formal Paα line fit for cB58 yields a flux of $(-0.2 \pm 2.3) \times 10^{-16}$ erg s$^{-1}$ cm$^{-2}$, from which we determined the Paα flux limit to be $<2.3 \times 10^{-16}$ erg s$^{-1}$ cm$^{-2}$, which agrees with the non-detection reported by Siana et al. (2008), $<6 \times 10^{-16}$ erg s$^{-1}$ cm$^{-2}$. The formal Brα line fit yields a line flux of $(-0.4 \pm 1.3) \times 10^{-16}$ erg s$^{-1}$ cm$^{-2}$, thus we report a limit of $<1.3 \times 10^{-16}$ erg s$^{-1}$ cm$^{-2}$.

The formal fit to Paα line flux of the Clone yields $(0.3 \pm 1.3) \times 10^{-16}$ erg s$^{-1}$ cm$^{-2}$, from which we report an upper limit similar to that of cB58 above. In the panel showing the Paα wavelength region for the Clone in Figure 4, we note a spectral feature at 5.9 $\mu$m (1.96 $\mu$m rest frame) that resembles a Paα line at $z \sim 2.1$. However, the spectroscopic redshift of 2.0026 was measured with multiple optical lines (Hainline et al. 2009) and thus precludes the possibility of the feature being interpreted as the Paα line. It is also unlikely to be an H$_2$ emission line at 1.96 $\mu$m given the absence of other H$_2$ lines nearby (2.03 and 2.12 $\mu$m). The source of the apparent feature therefore remains unknown.

### 3.2. Metallicity

We estimate metallicity with the N2 index (Pettini & Pagel 2004) using both linear and third-order fits (Table 6). The index is not affected by the optical extinction given the proximity of the lines. Both estimators yield consistent values, which agree well with those found by Erb et al. (2006) for massive galaxies at $z \gtrsim 2$ selected via UV luminosity. The range of the metallicity found in our sample is also in good agreement with the sample of 28 lensed galaxies at $1.5 < z < 5$ observed by Richard et al. (2011), $8.00 \geqslant Z \geqslant 8.94$, with an average oxygen abundance of $Z = 8.55$, similar to the average value from the linear N2 index in this work, $Z = 8.56$. That is, our sample has typical oxygen abundance for field and lensed galaxies at similar $z$.

### 3.3. Infrared Luminosity and Star Formation Rate

We can measure the SFR from $L$(TIR), which in turn can be estimated by three tracers: (1) far-IR SED fitting, (2) the monochromatic 24 $\mu$m $L$(TIR) estimator given by Rujopakarn et al. (2012), and (3) PAH emission line luminosity. The SFR can also be estimated from the Hα luminosity as well as the combination of Hα and 24 $\mu$m luminosity. We adopt the SFR derived from the SED-fitted $L$(TIR) as a fiducial for comparison. SFRs are calculated from $L$(TIR) by the relationship given by Rujopakarn et al. (2012). All SFR estimates are converted from their respective IMF assumptions to the Kroupa (2002) IMF. The SFR results are presented in this section and their implications are discussed in Section 4.

The far-IR SED fitting (e.g., 30 $\mu$m to $\sim$1 mm) is the most straightforward among the methods to measure $L$(TIR). However, far-IR photometry is often affected by confusion noise at longer wavelengths in crowded fields, thus limiting the applicability of far-IR SED fitting in deep cosmological surveys. The far-IR and submillimeter photometry in our sample is aided by magnification of the gravitational lenses and thus we can probe fluxes below the typical confusion limit of the instrument. The SED fitting for the $L$(TIR) for A2218b and A1835a were carried out by Rigby et al. (2008) by combining the 24 and

70 $\mu$m data with submillimeter observations, including at least 450 and 850 $\mu$m for all their galaxies and additionally 1.3 mm for A1835a. The value for A2218a is measured using *Herschel* observations by Finkelstein et al. (2011). The SED-fitted $L$(TIR) for the Clone and cB58 were from the Fadely et al. (2010) and Siana et al. (2008) studies, respectively. A2667a and the 8 O'clock arc have no $L$(TIR) estimates from far-IR SED fitting because the longest band we presently have is 70 $\mu$m. The 70 $\mu$m imaging for the latter is complicated by a nearby bright dust-obscured galaxy (Section 2.6) that blends with the arc.

The monochromatic (i.e., single-band) 24 $\mu$m $L$(TIR) estimator from Rujopakarn et al. (2012) yields $L$(TIR) consistent with the far-IR SED fitting at $0 < z < 2.8$ within 0.02 dex, on average, with a scatter of 0.12 dex for individual star-forming galaxies. Rujopakarn et al. (2012) take into account the evolution of the bolometric correction from local galaxies out to $z = 2.8$ (the farthest redshift where the 24 $\mu$m band traces predominantly dust and PAH emissions) due to the structural differences of IR galaxies by using the IR surface brightness, $\Sigma_{L(\mathrm{TIR})}$, as an indicator of IR SED, which has been demonstrated by Rujopakarn et al. (2011). Specifically, high-$z$ IR galaxies are physically extended and typically have 100–1000$\times$ more surface area than local counterparts at similar $L$(TIR) (Rujopakarn et al. 2011), and thus larger PAH-emitting area, which affects the bolometric corrections in the PAH wavelength region that is probed by the 24 $\mu$m band, particularly at $z > 1$ (Rujopakarn et al. 2012). We report the values of $L$(TIR) from this 24 $\mu$m indicator along with those from SED fitting in Table 5. The agreement between the monochromatic indicator and the far-IR SED fitting is within 0.12 dex (average difference of 0.06 dex), similar to the agreement reported in Rujopakarn et al. (2012). No systematic trends in redshift, luminosity, or metallicity are observed.

The last $L$(TIR) estimator is derived via the luminosity of the 6.2 $\mu$m PAH emission line, following the relationship given by Pope et al. (2008), which was measured by combining a local sample from Brandl et al. (2006) and the results for their submillimeter galaxies (SMGs). Pope et al. (2008) report a slope of the relationship between log 6.2 $\mu$m PAH luminosity and log $L$(TIR) to be approximately unity (formal slope $= 1.01 \pm 0.01$) over $L$(TIR) ranging from $10^{10}$ to $10^{13}$ $L_\odot$. Our objects are shown in Figure 6 on top of data points from Pope et al. (2008) and Brandl et al. (2006). The 24 $\mu$m $L$(TIR) values are used here instead of those from the far-IR SED fitting because A2667a has no far-IR $L$(TIR) estimate. Because of the methodological differences in the PAH flux measurements between Pope et al. (2008) and ours, particularly the assumption of the continuum level, for the purpose of the comparison in Figure 6, we normalize the PAH luminosity by a factor determined by matching our 6.2 $\mu$m PAH luminosity of cB58 to the measurement of the same object by Siana et al. (2008), who adopt the same continuum assumption as Pope et al. (2008). The 6.2 $\mu$m PAH feature was chosen to represent the aromatic emissions over other stronger PAH emission lines and emission complexes because it is narrow and relatively isolated from other lines, which mitigates the systematic uncertainties introduced by the process of deblending contributions from adjacent lines (which is required for, e.g., the 7.7 $\mu$m complex and 8.6 $\mu$m line). To estimate the SFR from the 6.2 $\mu$m PAH luminosity, the PAH luminosity is first converted to $L$(TIR) via the Pope et al. (2008) conversion and then to SFR via the Rujopakarn et al. (2012) relation.

In addition to estimating SFR via $L$(TIR), we also show the Kennicutt (1998) formula for Hα (no extinction correction)

**Table 5**
Derived Quantities

| Source | LIR (log $L_\odot$) | | SFR ($M_\odot$ yr$^{-1}$) | | | | | $A_\mathrm{v}^{\mathrm{H}\alpha/Spitzer}$ | $A_\mathrm{v}^{\mathrm{IR}}$ | $A_v$ |
|---|---|---|---|---|---|---|---|---|---|---|
| | 24 $\mu$m (1) | Far-IR SED (2) | H$\alpha$ (3) | H$\alpha$ + 24 $\mu$m (4) | PAH$_{6.2\,\mu m}$ (5) | LIR$_{24\,\mu m}$ (6) | LIR$_{\mathrm{Far-IRSED}}$ (7) | (8) | (9) | (10) |
| A2218b | 11.69 | 11.68 | 10.3 | 36.6 | 66.7 | 48.0 | 46.8 | 2.8 ± 0.3 | 2.1 | 2.5 |
| A2667a[a] | 11.68 | . . . | 13.9 | 39.9 | 19.4 | 47.1 | . . . | −2.4[a] ± 3.1 | 1.7 | −0.4 |
| The Clone[b] | 11.20 | 11.38 | 11.4 | 20.0 | 36.2 | 15.1 | 23.2 | <−1.1[b] | 1.0 | 1.0 |
| A2218a | 11.81 | 11.83 | 7.5 | 42.3 | 170.2 | 63.8 | 66.5 | 3.3 ± 0.4 | 3.0 | 3.2 |
| A1835a | 12.71 | 12.83 | 14.5 | 298 | 558.2 | 561 | 752 | 5.9 ± 0.4 | 5.4 | 5.7 |
| cB58[b] | 11.04 | 11.04 | 13.6 | 19.8 | 26.6 | 10.4 | 10.4 | <0.7[b] | −0.4 | −0.4 |
| 8 O'clock | 12.17 | . . . | 71.5 | 154 | . . . | 149 | . . . | 2.8 ± 0.3 | 1.0 | 1.9 |

**Notes.** Quantities in this table are corrected for lensing magnification. Column 1: $L$(TIR) estimated from the monochromatic 24 $\mu$m indicator from Rujopakarn et al. (2012). Column 2: $L$(TIR) measured by fitting SED to far-IR and submillimeter photometry. The values for A2218b and A1835a are from Rigby et al. (2008). The values for A2218a, the Clone, and cB58 are from Finkelstein et al. (2011), Fadely et al. (2010), and Siana et al. (2008), respectively. Column 3: H$\alpha$ SFR estimated by the Kennicutt (1998) formula (no extinction correction). Column 4: extinction-corrected SFR estimated using the H$\alpha$ and rest-frame 24 $\mu$m luminosity formula provided by Kennicutt et al. (2009). Column 5: SFR estimated by the PAH 6.2 $\mu$m complex luminosity. Column 6: SFR estimated by 24 $\mu$m monochromatic indicator provided by Rujopakarn et al. (2012). Column 7: SFR estimated using the far-IR $L$(TIR) in Column 2 and the relationship given by Rujopakarn et al. (2012). Column 8: screen extinction $A_v$ in mag estimated with H$\alpha$ and IR recombination lines assuming case-B recombination scenario. The value for cB58 uses H$\alpha$ and the Pa$\alpha$ line, the Br$\alpha$ limit for cB58 indicates an extinction limit of $A_v < 1.8$ mag. Column 9: $A_\mathrm{v}^{\mathrm{IR}}$ in mag. See Section 3.4 for more details. Column 10: final extinction estimate from averaging values in Columns 8 and 9. For cB 58 and the Clone, the $A_\mathrm{v}^{\mathrm{IR}}$ values are adopted.
[a] IR recombination line detected at low significance.
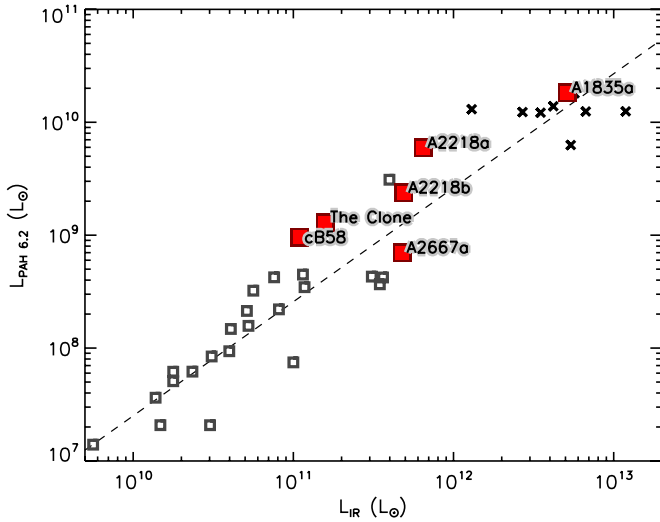[b] IR recombination line not detected.



**Figure 6.** Relationship of 6.2 $\mu$m PAH emission line luminosity to $L$(TIR) in our sample (large red squares) compared to the local star-forming galaxies and LIRGs from the Brandl et al. (2006) study (squares) and the high-redshift submillimeter galaxies from Pope et al. (2008, crosses). The dashed line is a linear relationship between log luminosities with slope of 1.01 measured by Pope et al. (2008). Our galaxies fall within this relationship, confirming the approximately unity slope reported by Pope et al. at the intermediate luminosities between the local and SMG samples.

(A color version of this figure is available in the online journal.)

and the Kennicutt et al. (2009) indicator that combines H$\alpha$ and the rest-frame 24 $\mu$m luminosity in order to correct for dust extinction in the SFR estimates. The SFR estimates from each method are tabulated in Table 5. We discuss the effects of extinction on the SFR estimates in Section 4.

### 3.4. Extinction

Extinctions derived from optical lines (e.g., H$\alpha$/H$\beta$) could suffer systematic underestimation where the overall extinction is large and the dust is mixed with the sources. This possibility

**Table 6**
Metallicity Estimates from [N II]/H$\alpha$

| Source | $Z_{\mathrm{PP04}}$ (1) | $Z_{\mathrm{PP04,3^{rd}order}}$ (2) |
|---|---|---|
| A2218b | 8.55 ± 0.04 | 8.53 ± 0.10 |
| A2667a | 8.67 ± 0.05 | 8.73 ± 0.10 |
| The Clone | 8.49 ± 0.02 | 8.45 ± 0.07 |
| A2218a | 8.55 ± 0.10 | 8.52 ± 0.25 |
| A1835a | 8.75 ± 0.15 | 8.91 ± 0.33 |
| cB58 | 8.31 ± 0.10 | 8.26 ± 0.35 |
| 8 O'clock | 8.58 ± 0.04 | 8.57 ± 0.09 |

**Notes.** Values are in 12+ log(O/H). Column 1: metallicity estimates from the N2 linear formula provided by Pettini & Pagel (2004). Column 2: metallicity estimates from the N2 third-order estimator from Pettini & Pagel (2004).

can be tested with IR recombination lines that are more robust to high extinction (Alonso-Herrero et al. 2006). To obtain a fiducial estimate, we assume a foreground screen and measure the extinction relative to H$\alpha$ using the Pa$\alpha$ and Br$\alpha$ lines assuming case-B recombination. For instance, for Br$\alpha$, the $A_\mathrm{v}^{\mathrm{H}\alpha/Spitzer}$ is given by

$$\frac{I_{\mathrm{Br}\alpha}}{I_{\mathrm{H}\alpha}} = \frac{I_{\mathrm{Br}\alpha,0}}{I_{\mathrm{H}\alpha,0}}\exp\left[-\frac{A_\mathrm{v}^{\mathrm{H}\alpha/Spitzer}}{1.086}(A_{\mathrm{Br}\alpha} - A_{\mathrm{H}\alpha})\right], \quad (1)$$

where $I_{\mathrm{Br}\alpha,0}/I_{\mathrm{H}\alpha,0} = 0.0291$ and for Pa$\alpha$, $I_{\mathrm{Pa}\alpha,0}/I_{\mathrm{H}\alpha,0} = 0.1226$ (Osterbrock & Ferland 2006) for $T_e = 10{,}000$ K at the low-density limit. The $A_{\mathrm{H}\alpha}$, $A_{\mathrm{Pa}\alpha}$, and $A_{\mathrm{Br}\alpha}$ are given by interpolation using the Rieke & Lebofsky (1985) extinction law, which for $A_v$ of 1 mag are 0.8 mag, 0.15 mag, and 0.04 mag, respectively.

Alternatively, the extinction can be estimated from the optical and IR SFR values by taking the latter to be a fiducial SFR. The assumption is secure in our sample of IR luminous galaxies, where direct UV leakage from the galaxy is expected to be small (Rieke et al. 2009, and references therein). This alternative

extinction estimate, $A_v^{\mathrm{IR}}$, following Choi et al. (2006) is

$$A_{\mathrm{H}\alpha}^{\mathrm{IR}} = 2.5\log\left(\frac{\mathrm{SFR_{IR}}}{\mathrm{SFR_{H\alpha}}}\right). \qquad (2)$$

The $A_{\mathrm{H}\alpha}^{\mathrm{IR}}$ can then be converted to the $A_v^{\mathrm{IR}}$ via the Rieke & Lebofsky (1985) extinction law. When available, we use the far-IR $\mathrm{SFR_{IR}}$ to calculate the $A_v^{\mathrm{IR}}$, otherwise the value estimated from the 24 $\mu$m $L(\mathrm{TIR})$ is used.

The $A_v^{\mathrm{H}\alpha/Spitzer}$ method assumes a foreground screen of dust and therefore is a lower limit, whereas the $A_v^{\mathrm{IR}}$ does not. The comparison of measurements from both methods, tabulated in Table 5, shows that in three out of four galaxies where IR recombination lines are well detected (A2218b, A2218a, and A1835a), both methods agree within the range of uncertainty, which suggests that the nature of the dust distribution in these galaxies is roughly uniform, resembling the foreground screen assumption. The other object with a well-detected Pa$\alpha$ (the 8 O'clock arc), however, shows a 1.8 mag difference between $A_v^{\mathrm{H}\alpha/Spitzer}$ and $A_v^{\mathrm{IR}}$. The latter disagreement indicates an inhomogeneous mixture of dust in the 8 O'clock arc and highlights the diversity of the dust distribution scenarios at redshift $1 < z < 3$.

A2218a, A1835a, cB58, the Clone, and the 8 O'clock arc have extinction measurements from optical and/or rest-frame optical spectroscopy in the literature that can be compared with our IR measurements. Richard et al. (2011) found $E(B-V)_{\mathrm{star}}$ of 0.18 for A2218a from SED fitting, implying $A_v$ of 0.6 mag, assuming the $R = 3.1$ law. A1835a has extinction measurements by Nesvadba et al. (2007) using H$\alpha$/H$\beta$ ratio of $E(B-V) = $ 1.3–1.6, implying $A_v$ of 4.0–5.0 mag. Teplitz et al. (2000) measured $E(B-V)$ of 0.27 for cB58 from the H$\alpha$/H$\beta$ line ratio, implying $A_v$ of 0.4 mag. For the Clone, Hainline et al. (2009) measured $E(B-V)$ using the H$\alpha$/H$\gamma$ line ratio to be 0.28, which implies $A_v$ of 0.9 mag. The extinction of the 8 O'clock arc was measured by Finkelstein et al. (2009) using a weighted mean of H$\alpha$, H$\beta$, and H$\gamma$ line ratios to be $A_v = 1.17 \pm 0.36$ mag (using only H$\alpha$/H$\beta$ yields $E(B-V)_{\mathrm{gas}}$ of 0.97, implying $A_v$ of 1.3 mag); and by Dessauges-Zavadsky et al. (2011) to be $E(B-V)_{\mathrm{gas}} = 0.30 \pm 0.04$ mag, implying $A_v$ of 0.9 mag. From Table 5, the extinction measurements from IR recombination lines for A2218a, A1835a, and the 8 O'clock arc, where we have secure IR line detections, are $3.3 \pm 0.4$ mag, $5.9 \pm 0.4$ mag, and $2.8 \pm 0.3$ mag, respectively. While our sample size is too small to draw a general conclusion, the comparison suggests that the optical measurements may sample systematically lower extinction regions, in agreement with local LIRGs and ULIRGs (e.g., Alonso-Herrero et al. 2006).

The $A_v^{\mathrm{H}\alpha/Spitzer}$ values for A2667a and the Clone are negative because the formal fits to the Pa$\alpha$ and Br$\alpha$ line yield values (or flux limits) lower than those expected for the extinction of 0 mag (as shown in the simulated $A_v$ in Figures 3 and 4); the line is undetected), albeit with a considerable uncertainty. For cB58, the line flux for both Pa$\alpha$ and Br$\alpha$ are negative and thus the $A_v^{\mathrm{H}\alpha/Spitzer}$ cannot be formally calculated and we report a $1\sigma$ upper limit as cB58's $A_v^{\mathrm{H}\alpha/Spitzer}$. Given the general agreement between $A_v^{\mathrm{H}\alpha/Spitzer}$ and $A_v^{\mathrm{IR}}$ in a majority of objects with secure measurements of Pa$\alpha$ and Br$\alpha$, we adopt an average value of $A_v^{\mathrm{H}\alpha/Spitzer}$ and $A_v^{\mathrm{IR}}$ as a representative value of $A_v$ (except for the cB58 and the Clone for which we adopt the $A_v^{\mathrm{IR}}$ value).
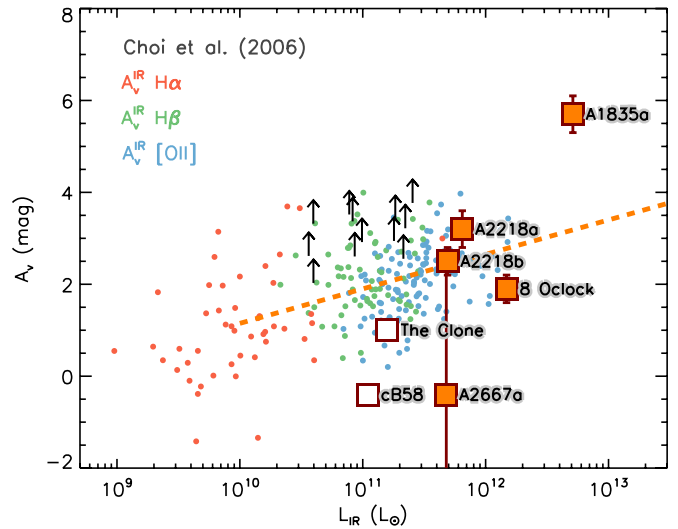


**Figure 7.** Optical extinction, $A_v$, from this work compared to the distribution of Choi et al. (2006) from the *Spitzer* First-Look Survey (FLS) with mean redshift of $z = 0.8$. Our points are shown in filled squares, except for the cB58 point (empty square), where we adopt the $A_v^{\mathrm{IR}}$ value as an extinction estimate (see Section 3.4). The Choi et al. (2006) points are $A_v^{\mathrm{IR}}$ measured by comparing the IR SFR, which is taken as a fiducial value, with the optical SFR measured from the H$\alpha$, H$\beta$, and [O II] emission lines. These are shown in red, blue, and gray circles, respectively. The intrinsic spread of points toward higher extinction of the Choi et al. sample may be larger if the line non-detections (upward arrows), which are likely due to large extinction, could have been measured. The intrinsic spread of extinction at high-$z$ is far wider than previously known from optical-based measurements.

(A color version of this figure is available in the online journal.)

We present our final $A_v$ estimates as a function of $L(\mathrm{TIR})$ from the 24 $\mu$m indicator in Figure 7. Again, the 24 $\mu$m $L(\mathrm{TIR})$ is used here because A2667a and the 8 O'clock arc lack far-IR $L(\mathrm{TIR})$ estimates. Our measurements are compared with the $A_v^{\mathrm{IR}}$ measurements by Choi et al. (2006), who study the extinctions of objects selected in the near-IR and mid-IR from the *Spitzer* First Look Survey (FLS), which have a mean redshift of $z = 0.8$ and luminosities ranging from the sub-LIRG to ULIRG range. Their extinction measurements are obtained by comparing the SFR estimates from the H$\alpha$, H$\beta$, and [O II] line fluxes with those from IR luminosities. That is, they estimated the extinction using the ratio of SFR from the individual optical indicators to the IR SFR estimates, e.g., $\mathrm{SFR_{H\alpha}}/\mathrm{SFR_{IR}}$, $\mathrm{SFR_{H\beta}}/\mathrm{SFR_{IR}}$, etc. The Choi et al. distribution of extinction values shows a correlation between $A_v^{\mathrm{IR}}$ and $L(\mathrm{TIR})$ with a formal fit of $A_v^{\mathrm{IR}} = 0.75 \times \log L(\mathrm{TIR}) - 6.35$, shown as the orange line in Figure 7. The scatter is $\sim 0.8$ mag; however, this value does not include cases where [O II] is undetected (shown as lower limits in Figure 7). Allowing for these limits, the scatter is $\gtrsim 1$ mag. This fit and the large scatter are similar to the result of Afonso et al. (2003), who estimate extinction by comparing H$\alpha$ and [O II] SFR estimates to those from the 1.4 GHz radio continuum at a similar mean redshift of $z = 0.8$. A number of authors (e.g., Bai et al. 2007; Kocevski et al. 2011) find that the variations in extinction are so large that [O II] can be difficult to detect in some galaxies that have high SFRs indicated at 24 $\mu$m, although with high-quality spectra there are relatively few cases where [O II] is completely absent (Weiner et al. 2007).

We found the spread of our extinction values to be at least as large. A2218a, A2218b, and the 8 O'clock arc lie within the uncertainties of the Choi et al. relationship. A2667a and cB58, with nearly zero mag extinction, are less obscured for
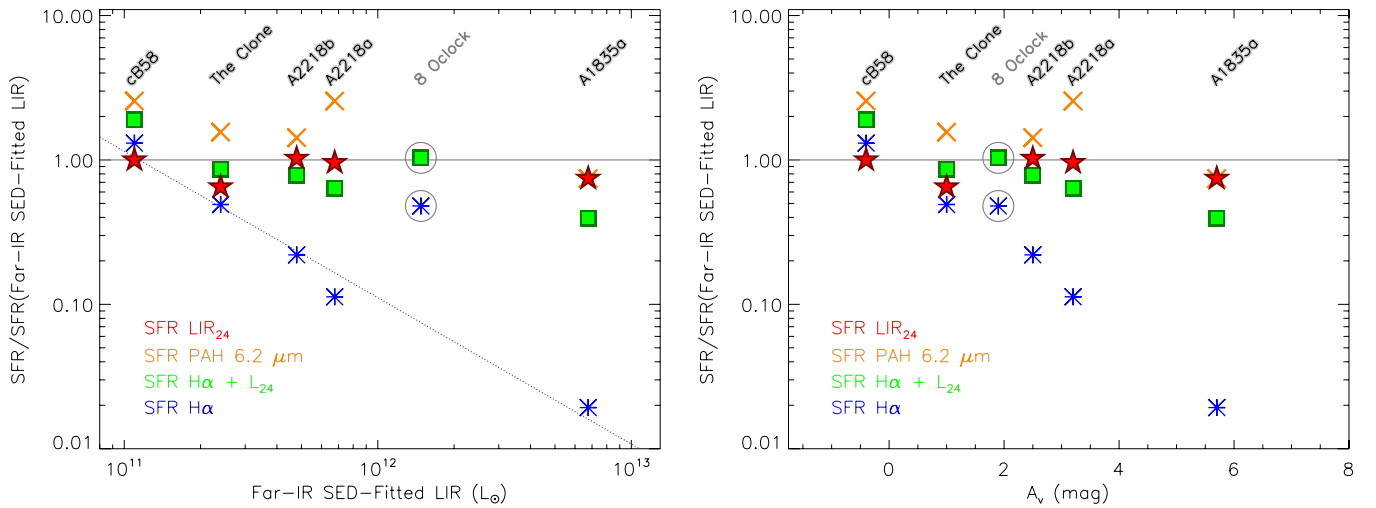
**Figure 8.** Comparison of star formation rate (SFR) estimated from the uncorrected Hα, Hα + rest-frame $L(24\,\mu m)$, $L$(TIR) from 24 μm indicator, and $L$(TIR) from the 6.2 μm PAH emission line, to the SFR estimated from far-IR SED fitted $L$(TIR), which is taken as a fiducial value, as a function of $L$(TIR) and $A_v$, shown in the left and right panels, respectively. The Hα SFR indicator systematically underestimates $L$(TIR) with increasing discrepancy from the fiducial at larger $L$(TIR)), while the rest are consistent to the fiducial within the range of uncertainties. A trend line for the extinction effect on the Hα SFR indicator in objects with a screen-like extinction scenario (Section 4) is shown as the blue dotted line. The points representing the 8 O'clock arc are circled in gray to indicate that $L$(TIR) of the arc is estimated from 24 μm because the SED-fitted $L$(TIR) is not available. The deviation of Hα SFR of the arc from the trend line in the left panel, however, is not due to the $L$(TIR) measurement, but rather the differences of dust distribution scenarios between the inhomogeneous mixture in the arc and the homogeneous distribution in the rest of the sample (see Section 3.4).

(A color version of this figure is available in the online journal.)

their $L$(TIR), whereas the extinction of A1835a is far above the relationship. Selection effects may have reduced the scatter in many previous studies (e.g., the need to have an [O II] line of measurable strength). Our results indicate that galaxies up to $z \sim 3$ show a very large range of $A_v$, as is the case in the local universe.

## 4. EFFECTS OF EXTINCTION ON STAR FORMATION RATE INDICATORS

In Figure 8, we compare the SFR estimates from Hα (un-corrected for dust extinction), Hα + $L(24\,\mu m)$, $L(24\,\mu m)$, and the 6.2 μm PAH emission with those of $L$(TIR) measured by far-IR SED fitting as a function of $L$(TIR) (Figure 8, left) and $A_v$ (Figure 8, right). A2667a is excluded from this comparison due to its lack of the far-IR SED fitted $L$(TIR) and the fact that the curvature of the lensed arc caused a fraction of Hα flux to fall off the slit (the position of the slit is shown in the bottom left panel of Figure 1; a part of the "A2" arc is outside the slit). Without the correction for dust extinction, the Hα SFR indicator is clearly affected at high $L$(TIR) and extinction. For the cases that extinction behavior resembles a uniform dust screen (every galaxy except the 8 O'clock arc), there is a tight trend of the Hα SFR deviation from the fiducial SED-fitted SFR as a function of the log[$L$(TIR)] that is given by

$$\log[\mathrm{SFR}(\mathrm{H}\alpha)/\mathrm{SFR}(\mathrm{LIR})] = 11.21 - 1.01\log[L(\mathrm{TIR})]. \quad (3)$$

Applying a single overall extinction to Hα will increase the estimates of SFRs and improve the agreement to the $L$(TIR) SFR, but will not correct the trend with $L$(TIR). Further improvement in Hα-based SFRs require introducing corrections for extinction as a function of stellar mass (e.g., Moustakas et al. 2006; Weiner et al. 2007), or of the SFR itself (e.g., Buat et al. 2005); see Section 4.

The deviation of the Hα point of 8 O'clock arc in Figure 8 (left) indicates that a larger amount of Hα flux is

escaping from the arc given its $L$(TIR), which could be due to a different dust distribution relative to the star-forming regions. The indicator is usually applied with a single nominal level of extinction; in this case, the line in Figure 8 (left) would be shifted upward but the slope would not be corrected.

For A2218a, A1835a, and the 8 O'clock arc where Paα line is well detected, we apply the extinction correction to the Paα line luminosity and compare the ratio of $L(24\,\mu m)/L(\mathrm{Pa}\alpha_{\mathrm{corr}})$ with the relationship that Alonso-Herrero et al. (2006) found for local LIRGs. Papovich et al. (2009) made this comparison for A2218a and found the $L(24\,\mu m)/L(\mathrm{Pa}\alpha_{\mathrm{corr}})$ ratio to be $\simeq 0.5$ dex lower than the local relation, indicating that A2218a has lower $L(24\,\mu m)$ than local galaxies of comparable $L(\mathrm{Pa}\alpha_{\mathrm{corr}})$, while agreeing with those of local individual H II regions. Papovich et al. interpreted this difference as an indication that A2218a harbors extended star-forming regions similar to a scaled-up local H II regions, rather than nuclear starburst like local U/LIRGs. In our analysis, we have reproduced the $L(24\,\mu m)/L(\mathrm{Pa}\alpha_{\mathrm{corr}})$ ratio measured by Papovich et al. using our reduction technique for A2218a, $\log[L(24\,\mu m)/L(\mathrm{Pa}\alpha_{\mathrm{corr}})] = 2.2 \pm 0.2$, and also found that the ratio for A1835a and the 8 O'clock arc are 0.9–1.1 dex lower than the Alonso-Herrero et al. (2006) relationship. This is consistent with the result in Table 5 that the Rujopakarn et al. (2012) single-band 24 μm $L$(TIR) indicator yields $L$(TIR) values that agree with the far-IR SED-fitted $L$(TIR), which implies that these galaxies have extended star formation (see Section 3.3 for details of the indicator). That is, the local relationship of $L(\mathrm{Pa}\alpha_{\mathrm{corr}})$ and $L(24\,\mu m)$ reported by Alonso-Herrero et al. (2006) could have limited applicability at high redshift because the Paα line will systematically have lower extinction for a given $L(24\,\mu m)$ due to the extended structure of star formation.

All the other indicators give consistent estimates, within the expected errors of ~0.2 dex. We found that the Hα + $L(24\,\mu m)$ indicator by Kennicutt et al. (2009) tends toward a smaller value

of SFR at large extinctions or large $L$(TIR), particularly above $10^{12} L_\odot$, as observed in A1835a and the 8 O'clock arc. The SFR estimates from the $6.2 \mu$m PAH emission do not show a systematic trend with $L$(TIR), although the scatter is larger than with other indicators. The scatter for individual galaxies is $\sim 0.2$ dex, similar to the scatter of $L$(TIR) values we have found in Rujopakarn et al. (2012) at redshifts where the $24 \mu$m band probes the PAH emissions. Since these are high S/N measurements of an individual (i.e., relatively non-blended) PAH emission line, this result suggests that the Rujopakarn et al. (2012) SFR indicator has succeeded in correcting for the SED evolution.

## 5. CONCLUSIONS

We observed four strongly gravitationally lensed star-forming galaxies at $1 < z < 3$ with *Spitzer*/IRS and the LBT/ LUCIFER to obtain the mid-IR and near-IR spectroscopy. These observations are targeted to cover IR recombination lines, including H$\alpha$ in the near-IR and Pa$\alpha$ or Br$\alpha$ in the mid-IR. We include another three galaxies from the literature with similar suites of observations, yielding a total sample of seven galaxies. Our sample spans the redshift range of 1.03–2.73 and the $L$(TIR) range of $1.3 \times 10^{11} L_\odot$ to $7.0 \times 10^{12} L_\odot$.

The IR recombination line ratios are used to measure extinction that can probe deep into the highly obscured star-forming regions and thus provide an unbiased measure of extinction under the foreground screen assumption. Independently, we estimate the extinction by comparing the optical and IR SFRs, a method that does not make the foreground screen assumption. The results from the two methods are consistent in three out of four galaxies with good IR recombination line flux measurements, suggesting that the dust extinction in these galaxies is consistent with a foreground screen (i.e., uniform dust distribution). However, in the fourth case, the extinction estimates from two methods disagree by 1.8 mag, indicating a deviation from the uniform dust screen assumption, which suggests an inhomogeneous dust mixture. The extinction range of our sample (assuming a foreground screen) is $\sim 0.0$–5.9 mag, which is a larger spread than previously known for intermediate- and high-redshift galaxies based on measurements with optical emission lines. These results suggest a large diversity in both the extinction levels and dust distribution scenarios at high redshift.

We compare the performance of various SFR indicators over the extinction range and find that substantial extinction corrections are required for the H$\alpha$-based SFR indicator. The remaining indicators (1) combined H$\alpha$ and $L(24 \mu$m), (2) $L(24 \mu$m), and (3) PAH $(6.2 \mu$m) all give estimates consistent to within the expected uncertainties of $\sim 0.2$ dex.

## REFERENCES

Afonso, J., Hopkins, A., Mobasher, B., & Almeida, C. 2003, ApJ, 597, 269
Allam, S. S., Tucker, D. L., Lin, H., et al. 2007, ApJ, 662, L51
Alonso-Herrero, A., Rieke, G. H., Rieke, M. J., et al. 2006, ApJ, 650, 835
Bai, L., Marcillac, D., Rieke, G. H., et al. 2007, ApJ, 664, 181
Becker, G. D., Rauch, M., & Sargent, W. L. W. 2009, ApJ, 698, 1010
Berta, S., Magnelli, B., Nordon, R., et al. 2011, A&A, 532, A49
Bian, F., Fan, X., Bechtold, J., et al. 2010, ApJ, 725, 1877
Bouché, N., Lehnert, M. D., Aguirre, A., Péroux, C., & Bergeron, J. 2007, MNRAS, 378, 525
Brandl, B. R., Bernard-Salas, J., Spoon, H. W. W., et al. 2006, ApJ, 653, 1129
Buat, V., Iglesias-Páramo, J., Seibert, M., et al. 2005, ApJ, 619, L51
Choi, P. I., Yan, L., Im, M., et al. 2006, ApJ, 637, 227
Dessauges-Zavadsky, M., Christensen, L., D'Odorico, S., Schaerer, D., & Richard, J. 2011, A&A, 533, A15
Diamond-Stanic, A. M., & Rieke, G. H. 2010, ApJ, 724, 140
Diolaiti, E., Bendinelli, O., Bonaccini, D., et al. 2000, A&AS, 147, 335
Dole, H., Lagache, G., Puget, J.-L., et al. 2006, A&A, 451, 417
Engelbracht, C. W., Blaylock, M., Su, K. Y. L., et al. 2007, PASP, 119, 994
Erb, D. K., Shapley, A. E., Pettini, M., et al. 2006, ApJ, 644, 813
Fadely, R., Allam, S. S., Baker, A. J., et al. 2010, ApJ, 723, 729
Finkelstein, K. D., Papovich, C., Finkelstein, S. L., et al. 2011, ApJ, 742, 108
Finkelstein, S. L., Papovich, C., Rudnick, G., et al. 2009, ApJ, 700, 376
Hainline, K. N., Shapley, A. E., Kornei, K. A., et al. 2009, ApJ, 701, 52
Kennicutt, R. C. 1998, ARA&A, 36, 189
Kennicutt, R. C., Jr., Hao, C.-N., Calzetti, D., et al. 2009, ApJ, 703, 1672
Kneib, J.-P., Ellis, R. S., Smail, I., Couch, W. J., & Sharples, R. M. 1996, ApJ, 471, 643
Kneib, J.-P., van der Werf, P. P., Kraiberg Knudsen, K., et al. 2004, MNRAS, 349, 1211
Kobayashi, C., Springel, V., & White, S. D. M. 2007, MNRAS, 376, 1465
Kocevski, D. D., Lemaux, B. C., Lubin, L. M., et al. 2011, ApJ, 736, 38
Kroupa, P. 2002, Science, 295, 82
Le Floc'h, E., Papovich, C., Dole, H., et al. 2005, ApJ, 632, 169
Lin, H., Buckley-Geer, E., Allam, S. S., et al. 2009, ApJ, 699, 1242
Magnelli, B., Elbaz, D., Chary, R. R., et al. 2011, A&A, 528, A35
Mandel, H., Seifert, W., Lenzen, R., et al. 2007, Astron. Nachr., 328, 626
Moustakas, J., Kennicutt, R. C., Jr., & Tremonti, C. A. 2006, ApJ, 642, 775
Nesvadba, N. P. H., Lehnert, M. D., Genzel, R., et al. 2007, ApJ, 657, 725
Osterbrock, D. E., & Ferland, G. J. 2006, in Astrophysics of Gaseous Nebulae and Active Galactic Nuclei, ed. D. E. Osterbrock & G. J. Ferland (2nd ed.; Sausalito, CA: Univ. Science Books)
Papovich, C., Rudnick, G., Rigby, J. R., et al. 2009, ApJ, 704, 1506
Pérez-González, P. G., Rieke, G. H., Egami, E., et al. 2005, ApJ, 630, 82
Pettini, M., & Pagel, B. E. J. 2004, MNRAS, 348, L59
Pope, A., Chary, R.-R., Alexander, D. M., et al. 2008, ApJ, 675, 1171
Reddy, N. A., Steidel, C. C., Pettini, M., et al. 2008, ApJS, 175, 48
Richard, J., Jones, T., Ellis, R., et al. 2011, MNRAS, 413, 643
Rieke, G. H., Alonso-Herrero, A., Weiner, B. J., et al. 2009, ApJ, 692, 556
Rieke, G. H., & Lebofsky, M. J. 1985, ApJ, 288, 618
Rieke, G. H., Young, E. T., Engelbracht, C. W., et al. 2004, ApJS, 154, 25
Rigby, J. R., Marcillac, D., Egami, E., et al. 2008, ApJ, 675, 262
Rodighiero, G., Vaccari, M., Franceschini, A., et al. 2010, A&A, 515, A8
Rujopakarn, W., Eisenstein, D. J., Rieke, G. H., et al. 2010, ApJ, 718, 1171
Rujopakarn, W., Rieke, G. H., Eisenstein, D. J., & Juneau, S. 2011, ApJ, 726, 93
Rujopakarn, W., Rieke, G. H., Weiner, B. J., et al. 2012, arXiv:1107.2921
Sand, D. J., Treu, T., Ellis, R. S., & Smith, G. P. 2005, ApJ, 627, 32
Seitz, S., Saglia, R. P., Bender, R., et al. 1998, MNRAS, 298, 945
Siana, B., Teplitz, H. I., Chary, R.-R., Colbert, J., & Frayer, D. T. 2008, ApJ, 689, 59
Smail, I., Smith, G. P., & Ivison, R. J. 2005, ApJ, 631, 121
Smith, J. D. T., Draine, B. T., Dale, D. A., et al. 2007, ApJ, 656, 770
Teplitz, H. I., Desai, V., Armus, L., et al. 2007, ApJ, 659, 941
Teplitz, H. I., McLean, I. S., Becklin, E. E., et al. 2000, ApJ, 533, L65
Vacca, W. D., Cushing, M. C., & Rayner, J. T. 2003, PASP, 115, 389
Weiner, B. J., Papovich, C., Bundy, K., et al. 2007, ApJ, 660, L39
Yee, H. K. C., Ellingson, E., Bechtold, J., Carlberg, R. G., & Cuillandre, J.-C. 1996, AJ, 111, 1783